RESEARCH Open Access



Drought-driven declines in water-use efficiency reshape carbon dynamics of a subtropical forest

Brian Njoroge Mwangi^{1,2,3}, Wyckliffe Ayoma^{1,2,3}, Yuelin Li^{1,2,3*}, L. Adrian Bruijnzeel⁵, Juxiu Liu^{1,2,3}, Jun Zhang⁶, Dennis Otieno⁴, Lindsay Sikuku^{1,2,3}, Mengmeng Yang^{1,2,3}, Vincent Suba^{1,2,3}, Oluoch Emily Achieng^{1,2,3}, Iheme Okechukwu^{1,2,3}, Ayesha Akter^{1,2,3}, Sohel Rana^{1,2,3}, Guowei Chu^{1,2,3}, Qianmei Zhang^{1,2,3}, Xuli Tang^{1,2,3}, Ze Meng^{1,2,3} and Degiang Zhang^{1,2,3}

Abstract

Background Subtropical forests play a critical role in global carbon cycling but are highly sensitive to climate-driven precipitation and temperature variability. At China's Dinghushan Biosphere Reserve, observed warming (\pm 1.5 °C since 2002) and precipitation declines (8.2 \pm 1.3 mm/yr) exceed global subtropical averages, yet their combined effects on water-use efficiency (WUE) and carbon exchange remain poorly quantified.

Methods Using 21 years of eddy covariance and meteorological data (2002–2022), we analyzed WUE (defined as NEE/ET; $g \in Kg^{-1} H_2O$) responses to drought events classified via the standardized precipitation index (SPI).

Results The reserve experienced increasing drought frequency, with 7 extreme droughts (SPI ≤ -2.0) post-2010 versus 2 pre-2010. Soil moisture extremes (< 0.15 m³ m⁻³) reduced WUE by 2.35 g C kg⁻¹ H₂O. Carbon fluxes showed differential sensitivity: ecosystem respiration (RE) declined most sharply (-71.9×10^{-5} g C m⁻² s⁻¹) during extreme droughts, while gross primary productivity (GPP) exhibited non-linear reductions below a 1,200 mm yr⁻¹ precipitation threshold. Late-successional forests maintained 0.94 g C kg⁻¹ H₂O higher WUE than mid-successional stands during droughts, linked to deeper rooting systems (120±15 cm). The identified 3-year recovery lag suggests targeted reforestation during wet intervals (SPI ≥ 1.5) could enhance resilience.

Conclusion By establishing quantitative drought thresholds and revealing hydraulic versus non-hydraulic limitations, our findings provide actionable strategies for subtropical forest conservation under climate change.

Keywords Climate change, Water-use efficiency (WUE), Carbon flux, Standardized precipitation index (SPI), Subtropical forest, Drought resilience, Eddy covariance, Ecosystem respiration

*Correspondence: Yuelin Li yuelin@scib.ac.cn

Full list of author information is available at the end of the article



Introduction

Subtropical forests account for 25% of global forest carbon sinks (Lv et al. 2022), yet their responses to climate change-induced drought remain poorly quantified, particularly in East Asia's rapidly warming regions (Zheng et al. 2020). Two critical knowledge gaps persist: (1) the precipitation thresholds triggering non-linear declines in water-use efficiency (WUE), and (2) the differential sensitivity of gross primary productivity (GPP) versus ecosystem respiration (RE) to drought intensity, especially in systems with shallow, clay-rich ultisols. These gaps limit predictions of subtropical forest resilience under projected climate scenarios.

Prior work has established baseline WUE responses in tropical forests (Yang et al. 2021) and identified RE as potentially more drought-sensitive than GPP in waterlimited systems (Bassiouni & Vico 2021). However, these studies lacked long-term observational validation and mechanistic links to specific drought metrics like the standardized precipitation index (SPI). China's Dinghushan Biosphere Reserve presents an ideal study system to address these gaps, with its 21-year eddy covariance record, characteristic shallow acidic soils (pH 4.0-4.9; Huang et al. 2021), and strong ENSO-modulated precipitation variability (Yuan et al. 2010). Previous research at this site focused mainly on seasonal carbon fluxes (Pan et al. 2023), leaving unanswered how different drought intensities alter WUE trajectories and carbon flux thresholds.

We hypothesize that: (1) WUE declines follow a two-phase pattern, initial stomatal control dominance (moderate drought) shifting to non-stomatal limitation dominance (extreme drought, $SPI \le -2.0$) as observed in other Asian forests (Yang et al. 2021), and (2) RE shows greater sensitivity than GPP to prolonged droughts due to microbial activity suppression in Dinghushan's clayrich ultisols (Bassiouni & Vico 2021). Using SPI-quantified drought events from 2002 to 2022, we specifically test whether: (a) a 1,200 mm yr⁻¹ precipitation threshold triggers disproportionate WUE declines, and (b) drought legacy effects persist for>3 years post-recovery. This study advances the field by: (1) quantifying SPI-based drought thresholds for subtropical forest functioning, (2) revealing the hydraulic versus non-hydraulic controls on WUE across drought intensities, and (3) providing the first evidence of differential carbon flux sensitivity in Chinese subtropical forests, findings that directly inform China's Forest Resilience Plans.

Materials and methods

Study site description

The Dinghushan Biosphere Reserve (23° 09′ 21"–23° 11′ 30" N, 112° 30′ 39"–112° 33′ 41″ E) spans 1,156 ha

in Guangdong Province, China (Li et al. 2023). Elevation ranges from 100–1,000 m, with Jilong Mountain as the highest peak (1,000.3 m; Pan et al. 2023). The site's heterogeneous landscape (Fig. 1) includes rivers, coniferous, broadleaf, and mixed forests surrounding the central flux tower (23°10′24″N, 112°32′10″E).

The reserve experiences a humid subtropical climate with a mean annual temperature of 20.9 ± 0.2 °C (extreme range: 0.2 ± 0.21 °C to 38.0 ± 0.18 °C; Li et al. 2021). Seasonal extremes occur in July (28.8 ± 0.1 °C) and January (13.4 ± 0.1 °C). Annual precipitation averages 1,927 mm (1990-2020), with 81% occurring during the wet season (April–September; Li et al. 2023). ENSO-driven climate variability significantly modulates rainfall patterns, particularly affecting the Jiangnan region and Yangtze Basin (Yuan et al. 2010).

The mixed coniferous-broadleaf forest features 95% canopy density, with a mean tree height of $17\pm1.8~\text{m}$ and peak leaf area index (LAI) of $3.8-4.2~\text{m}^2~\text{m}^{-2}$ (Luo et al. 2022). Soils are classified as Ultisols (USDA system) derived from weathered sandstone and shale. These acidic soils (pH 4.0-4.9) contain $42\pm5\%$ clay in upper horizons and show significant surface humus accumulation (Huang et al. 2021). The soil's water retention capacity reaches $0.31~\text{m}^3~\text{m}^{-3}$ at saturation, with hydraulic conductivity three times higher in the topsoil (> 30 cm depth) compared to deeper layers (Liu et al. 2020).

Micrometeorological and eddy covariance measurements

The study utilized a 38-m eddy covariance flux tower installed in 2002 at the Dinghushan Biosphere Reserve, positioned on a 10° southeast-facing slope at 300 m elevation. The tower extended approximately 21 m above the mean forest canopy height to ensure adequate flux footprint representation. The core eddy covariance system consisted of an open-path infrared gas analyzer (LI-7500, LI-COR Biosciences, Lincoln, NE, USA) mounted at 36 m and a three-dimensional sonic anemometer (CSAT3, Campbell Scientific Inc., Logan, UT, USA) at 38 m height. Both instruments collected high-frequency data at 10 Hz, with flux calculations performed over 30-min intervals using EddyPro® 7 software (LI-COR, 2021). The LI-7500 analyzer underwent biweekly calibration checks using certified zero (100% N₂) and span (386 ppm CO₂) gases to maintain measurement accuracy.

Complementary meteorological measurements were collected from a 17-m instrument tower adjacent to the flux tower. This system included a quantum sensor (LI-190R, LI-COR) for photosynthetically active radiation (PAR) measurements, a combined temperature and relative humidity probe (HMP155, Vaisala, Helsinki, Finland), a wind monitor (05103, RM Young, Traverse City, MI, USA) for wind speed and direction, and a tipping

Mwangi et al. Ecological Processes

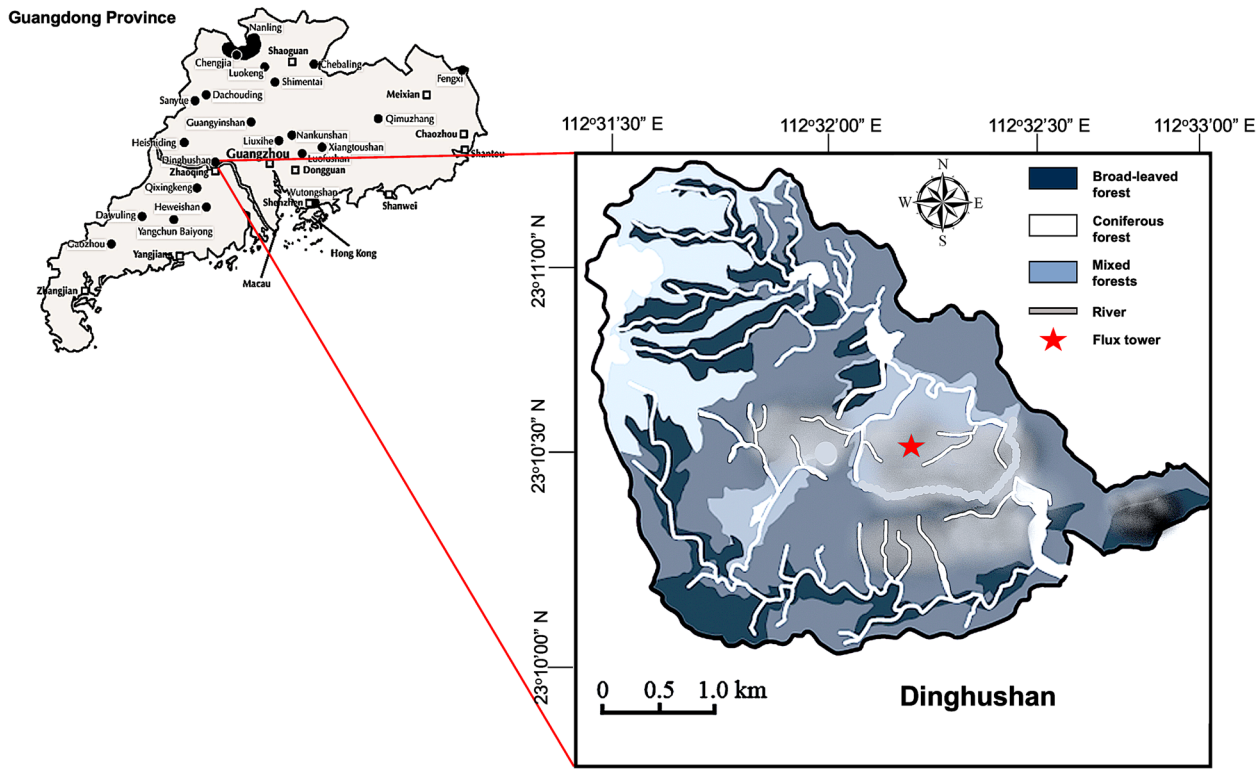


Fig. 1 Map of the Dinghushan Biosphere Reserve study site showing the spatial distribution of key features including the eddy covariance flux tower location (red star), forest types (broadleaf, coniferous, mixed), hydrological features (rivers, streams), and elevation contours (100–1000 m). The base map comes from the Dinghushan Station GIS database, with an inset showing the location within Guangdong Province, China

bucket rain gauge (TE525MM, Texas Electronics, Dallas, TX, USA) for precipitation monitoring. All meteorological sensors recorded data at 1-min intervals that were subsequently aggregated to 30-min means to match the flux calculation periods.

Canopy wetness conditions were monitored using three digital leaf wetness sensors (PHYTOS 31, METER Group, Pullman, WA, USA) installed at 4 m, 7 m, and 15 m heights on north-facing branches of dominant tree species. Sensors were mounted at 45° angles to approximate natural leaf orientation and minimize water droplet accumulation. The continuous wetness data, classified into four states (dry, mildly wet, fairly wet, and fully wet), were used to identify and exclude periods when canopy transpiration was negligible from water-use efficiency calculations.

A soil monitoring network consisting of six measurement stations provided continuous belowground data. Each station was equipped with time-domain reflectometry probes (CS616, Campbell Scientific) for soil moisture and thermocouples (109SS, Campbell Scientific) for soil temperature, both taking measurements at 5 cm, 20 cm, 40 cm, 80 cm, and 100 cm depths. All six soil moisture stations were installed within the flux tower's

dominant footprint area (80% contribution zone within a 300 m radius), with two stations co-located < 50 m from the tower base to ensure direct comparability with flux measurements. Spatial variation was quantified through monthly calibration checks across stations, showing consistent soil moisture values (±0.02 m³ m⁻³) except during extreme dry periods when microtopography caused slightly greater variation (± 0.04 m³ m⁻³). The strong soil moisture correlations with other variables in this study (SPI and WUE) reflect this spatial homogeneity, though we conservatively applied ± 10% uncertainty bounds to account for microsite differences. Data from all soil sensors were recorded at 10 Hz using CR23X dataloggers (Campbell Scientific) and processed to 30-min averages. The multi-depth configuration allowed characterization of vertical water and heat flux dynamics throughout the soil profile.

Standard CO₂ flux data processing

Quality control and corrections CO₂ flux data (2002–2022) were processed using standardized methods from global flux networks (Fine et al. 2022). Raw 10 Hz data underwent planar fit coordinate rotation (Finnigan 2004) and friction velocity (u*) filtering (threshold: 0.2 m s⁻¹;

Yu et al. 2021). The Webb-Pearman-Leuning (WPL) correction accounted for density effects on flux measurements (Sigid et al. 2023). Data were excluded when: (1) $u^* < 0.2 \text{ m s}^{-1}$, (2) precipitation occurred within 1 h, or (3) instrument diagnostics flagged errors.

Gap-filling procedures For flux gap-filling, we applied the marginal distribution sampling (MDS) algorithm following Reichstein et al. (2005), implemented via the REddyProc package (Wutzler et al. 2018). This approach preserves diurnal and seasonal covariance patterns by sampling from similar meteorological conditions and aligns with ChinaFLUX processing standards (Yu et al. 2018). Meteorological data gaps (<15% of records) were filled separately using REddyProc's mean diurnal variation (MDV) method, as met variables require less complex interpolation. The MDS algorithm was specifically chosen for fluxes due to its demonstrated reliability for eddy covariance datasets with similar climate regimes and vegetation types to ours (Wutzler et al. 2018).

Flux partitioning Nighttime net ecosystem exchange (NEE) was assumed equivalent to ecosystem respiration (RE; Eq. 1), an assumption that follows the widely used Reichstein et al. (2005) approach. Daytime RE was estimated using the Kok method (Kok 1948), which extrapolates respiration from the light-response curve at low irradiance (<50 µmol PPFD). Gross primary productivity (GPP) was derived as GPP = NEE + RE (Eq. 2). Partitioning uncertainty was assessed via 1000-iteration bootstrap resampling. While ReddyProc was employed for gap-filling due to its robust handling of missing meteorological data, flux partitioning was performed separately using the Kok method to better isolate daytime respiration (Kok 1948) and account for light inhibition effects specific to our forest type. NEE partitioning was performed in two stages: (1) Initial separation of RE and GPP using nighttime data (Reichstein et al. 2005), and (2) refinement of daytime RE using the Kok method to account for light inhibition. This hybrid approach was adopted because the Kok method better captures respiration dynamics during low-light conditions (<50 µmol PPFD), which are frequent in our dense canopy.

$$NEE_{nighttime} = RE_{nighttime}$$
 (1)

$$GPP = NEE + RE \tag{2}$$

Determination of water stress periods using SPI

SPI calculation The standardized precipitation index (SPI) was calculated monthly using Dinghushan's precipitation records (2002–2022) following Lloyd-Hughes &

Saunders (2002). A Gamma distribution was fitted to the data (Eq. 3):

$$SPI = \left\{ X_i - \overline{X} \right\} \{ \sigma \} \tag{3}$$

where X_i is monthly precipitation, \bar{x} is the 33-year mean (1990–2020), and σ is the standard deviation. Zero-precipitation months were adjusted using H(x) = q + (1 - Q)G(x), where q = P(x = 0). Computations used the WMO SPI software (v3.1) with a 3-month accumulation period to capture short-term water stress.

Drought classification Drought events were categorized by SPI thresholds:

Moderate drought: $-1.0 \le SPI < -1.49$ Severe drought: $-1.5 \le SPI < -1.99$ Extreme drought: $SPI \le -2.0$

Categories were validated against soil moisture measurements (<0.15 m³ m⁻³ during extreme droughts; r=0.72, p<0.01).

Validation and trends SPI uncertainty was quantified via 1000-iteration bootstrap resampling. Temporal trends were assessed using the Mann–Kendall test (Agbo et al. 2023), with Sen's slope estimating drought intensity changes. The 10-day lag between SPI declines and soil moisture anomalies was confirmed via cross-correlation analysis.

Trend analysis

Temporal trends in precipitation, temperature, and SPI (2002–2022) were assessed using the Mann–Kendall test (Agbo et al. 2023) and Sen's slope estimator. The nonparametric approach was chosen due to skewed data distributions (Shapiro–Wilk test, <0.05). Lag-1 autocorrelation (r_1) was calculated, with Trend-Free Pre-Whitening (TFPW) applied when r_1 exceeded the 95% confidence interval (Zhou et al. 2023). Sen's slope quantified trend magnitudes, reported as change per decade (e.g., mm yr⁻¹ for precipitation). All analyses used the modifiedmk R package (Zhou et al. 2023).

Water-use efficiency (WUE) calculations

Three complementary formulations of WUE were computed to assess ecosystem-scale carbon—water coupling under different drought conditions. The standard WUE was calculated as WUE $_{\rm nee}$ =NEE/ET (g C kg $^{-1}$ H $_2$ O), representing net ecosystem exchange per unit evapotranspiration. To isolate photosynthetic water-use efficiency independent of respiratory fluxes, we derived WUE $_{\rm gpp}$ =GPP/ET. Additionally, we implemented WUE $_{\rm ne}$ =(GPP—RE $_{\rm day}$)/ET to capture net daytime carbon. We calculated three WUE formulations to isolate different drivers: (1) WUE $_{\rm nee}$ for ecosystem-scale

carbon–water balance; (2) ${\rm WUE_{\rm gpp}}$ to exclude respiratory effects; and (3) ${\rm WUE_{\rm ne}}$ to focus on net daytime assimilation. Daytime fluxes (9:00-15:00 local time) were analyzed separately to capture peak photosynthetic activity, as recommended by Yu et al. (2018) and Keenan et al. (2013) for subtropical forests. These calculations were performed using the carbon flux values derived in Sect. "Standard CO2 flux data processing". All fluxes were quality-controlled following the ChinaFLUX processing pipeline, with GPP and RE_{day} partitioned from NEE using the nighttime-based Reichstein approach and daytime respiration modeled as a function of soil temperature and moisture. These alternative formulations enabled the separation of stomatal versus respiratory influences on apparent WUE patterns (Kuglitsch et al. 2008). Evapotranspiration (ET) was derived from the latent heat flux (LE) measured by the eddy covariance system, converted to mass flux using the latent heat of vaporization ($\lambda = 2.45$ MJ kg⁻¹), and adjusted for energy balance closure (EBC) following the ChinaFLUX protocol (Yu et al. 2018). EBC correction factors averaged 0.82 ± 0.05 across the study period. The EBC correction was applied uniformly to all ET data using the ChinaFLUX protocol's site-specific approach. The mean correction factor (0.82 ± 0.05) represents the long-term average (2002-2022) with minimal seasonal variation (±0.03) and no significant interannual trends (Sen's slope = 0.001 yr⁻¹, p = 0.21). This consistency reflects the stability of our flux tower's instrumentation and footprint characteristics. While EBC adjustments inherently introduce uncertainty, the small temporal variability in our correction factor suggests limited impacts on relative ET and WUE trends. For absolute ET values, we recommend applying the reported correction factor when comparing with other studies. For unit consistency across analyses, all CO2 fluxes (NEE, GPP, RE) were converted from µmol C m⁻² s⁻¹ to g C m⁻² s⁻¹ using the molar mass of carbon $(12.01 \text{ g mol}^{-1})$ (Yu et al. 2018).

Three formulations of ecosystem water-use efficiency were computed:

Standard WUE (net ecosystem scale):

$$WUE_{nee} = \frac{NEE}{ET} (gCkg^{-1}H_2O)$$
 (4)

where NEE is net ecosystem exchange (g C m⁻² s⁻¹) and ET is evapotranspiration (g H₂O m⁻² s⁻¹).

Gross WUE (photosynthetic water-use efficiency):

$$WUE_{gpp} = \frac{GPP}{ET} \tag{5}$$

GPP (gross primary productivity) was derived from NEE partitioning (Reichstein et al. 2005).

Net daytime WUE (accounting for daytime respiration):

$$WUE_{ne} = \frac{GPP - RE_{day}}{ET} \tag{6}$$

 ${
m RE_{day}}$ (daytime ecosystem respiration) was modeled using the Lloyd & Taylor (1994) temperature-response function scaled by soil moisture.

Forest succession classification and analysis

Successional stages were classified using a combination of forest inventory data and remote sensing metrics. Late-successional stands (n=9) were defined as areas with > 80 years of observed growth since disturbance, canopy closure > 95%, and mean leaf area index (LAI) > 4.0 measured via hemispherical photography (LI-1900, LI-COR). Mid-successional stands (n=9) represented 40–80 year old forests with LAI 3.0–4.0 and 80–95% canopy closure. Stand age was verified using historical aerial imagery (1950–2020). LAI calculation is shown in Eq. 7:

$$LAI = -\frac{ln(P(\theta))}{K(\theta)}\cos(\theta) \tag{7}$$

where $P(\theta)$ = gap fraction at zenith angle θ (measured via hemispherical photography), $K(\theta)$ = extinction coefficient (0.5 for spherical leaf angle distribution).

For WUE comparisons, we stratified eddy covariance flux footprints using a footprint climatology model (Kljun et al. 2015) to isolate periods when > 70% of fluxes originated from either late- or mid-successional stands. Differences in WUE (g C kg $^{-1}$ H₂O) between successional classes during drought (SPI \leq –1.0) were tested using one-way ANOVA with stand type as fixed effect and soil moisture as covariate (JMP Pro 16). Rooting depth distributions were validated using minirhizotron imaging (Bartz Technology) at 20 cm intervals to 2 m depth. Successional class WUE comparison was calculated using Eq. 8 below:

$$WUE_{diff} = \frac{1}{n} \sum_{i=1}^{n} (WUE_{late,i} - WUE_{mid,i})$$
 (8)

where WUE_{late}=mean WUE of late-successional stands, WUE_{mid}=mean WUE of mid-successional stands, n=paired observation periods (n=18). The test statistic was:

$$F = \frac{MS_{between}}{MS_{within}} \tag{9}$$

This approach enabled us to isolate the effects of successional stages while controlling for microclimate variation across the study area. All statistical models met assumptions of normality (Shapiro–Wilk test) and homoscedasticity (Levene's test).

Quantifying stomatal and non-stomatal limitations

To partition drought impacts on photosynthesis between stomatal and non-stomatal processes, we complemented eddy covariance data with:

- (1) Chlorophyll fluorescence Measured monthly (2015–2022) using a portable fluorometer (OS5p, Opti-Sciences) on sun-exposed leaves of 3 dominant species (Castanopsis fissa, Schima superba, Cryptocarya concinna). The maximum quantum yield of PSII $(F_{\rm v}/F_{\rm m})$ was predawn (n=15 leaves/species). Declines > 10% indicate non-stomatal damage (Hoshika et al. 2022).
- (2) Leaf $\delta^{13}C$ Analyzed annually from litterfall samples (n = 50/yr) to infer long-term stomatal limitation trends (Ellsworth et al. 2023).
- (3) Vc_{max} estimates Derived from light-response curves (LI-6800, LI-COR) during wet/dry seasons (n = 20/species). A > 20% Vc_{max} reduction signifies biochemical limitations (Bassiouni et al. 2021).

For $F_{\rm v}/F_{\rm m}$ measurements, leaves were dark-adapted for 30 min using leaf clips (Opti-Sciences) prior to predawn measurements to ensure complete relaxation of reaction centers. Vc_{max} estimations followed strict environmental controls: leaf chamber temperature was maintained at 25 ± 0.5 °C using the LI-6800 Peltier system, with relative humidity stabilized at $60\pm5\%$ to prevent stomatal artifacts. These protocols align with recent best practices for subtropical species (Hoshika et al. 2022; Bassiouni et al. 2021).

Statistical analysis

Relationships between hydroclimatic variables (SPI, soil moisture) and ecosystem responses (WUE, carbon fluxes) were analyzed using SigmaPlot® 14.5 (Systat Software) and R v4.3. For parametric tests, data met assumptions of normality (Shapiro–Wilk test, p > 0.05) and homoscedasticity (Levene's test, p > 0.1); non-normal data were log-transformed.

Key analyses included: (1) Threshold detection: piecewise regression identified breakpoints in WUE-precipitation relationships, (2) flux component sensitivity: linear mixed models (RE/GPP ~ SPI × Soil Moisture + (1Year)) with Satterthwaite degrees of freedom, (3) successional stage effects: One-way ANCOVA ($F_{1,16}=6.7$, p=0.01) compared WUE between late- and mid-successional stands, controlling for soil moisture, (4) post-hoc Tukey tests ($\alpha=0.05$) and 95% bootstrap CIs (1000 iterations) quantified differences. Smoothing splines ($\lambda=0.65$) visualized non-linear trends in CO₂ fluxes.

Results

Micrometeorological trends at Dinghushan Biosphere Reserve

Precipitation and soil moisture dynamics

The 21-year dataset (2002–2022) revealed significant hydroclimatic shifts (Fig. 2). Annual precipitation averaged 1,404.6 mm, with extremes ranging from 936.5 mm (2012 drought) to 1,988.9 mm (2008 wet year) (σ =210.3 mm, IQR=1,102–1,687 mm). Sen's slope analysis revealed a significant precipitation decline of 8.2±1.3 mm/yr (p<0.05) from 2002–2022 (Fig. 2a). Soil moisture tracked precipitation declines, averaging 0.23 m³ m³ but dropping to a record low of 0.12 m³ m³ in January 2014, a critical threshold for plant water stress in this ecosystem. Cross-correlation analysis showed soil moisture lagged precipitation by 10 days (r=0.72, p<0.01), reflecting delayed infiltration through Dinghushan's clay-rich upper layers.

Temperature and PAR trends Mean annual temperature (22.6 °C) exceeded the 33-year average (21.1 °C; p < 0.05), with the highest monthly value (23.6 °C) recorded in 2019 (Fig. 3). Photosynthetically active radiation (PAR) covaried with temperature (r=0.89, p<0.001), peaking at 595 μmol m⁻² s⁻¹ in June 2011 but showing no long-term trend (Sen's slope = 0.12 μmol m⁻² s⁻¹ yr⁻¹, p=0.21).

Key drought events SPI analysis identified 27 drought episodes (SPI ≤ -1.0), including 7 extreme droughts (SPI ≤ -2.0) post-2010 versus 2 pre-2010 (Table 1). The most intense event (SPI = -2.85, August–November 2012) corresponded with the lowest soil moisture (0.12 m³ m⁻³) and a 45.6% WUE reduction relative to wet years (p < 0.001, Tukey's HSD).

Temperature and PAR trends

The Dinghushan Biosphere Reserve exhibited significant warming over the 21-year study period (2002–2022). Mean annual temperature reached 22.6 °C (\pm 0.3 °C SD). Temperature extremes were recorded in July 2019 (23.6 °C) and January 2008 (22.1 °C), with wet-season months (April–September) averaging 3.2 °C warmer than dry-season months (paired t-test, p<0.01). This warming trend showed no significant correlation with annual precipitation totals (r=-0.12, p=0.34).

PAR demonstrated strong seasonal patterns, ranging from 120 µmol m⁻² s⁻¹ during cloudy conditions in March 2010 to 595 µmol m⁻² s⁻¹ in June 2011. PAR values showed tight coupling with air temperature (r=0.89, p<0.001), reflecting the dominant influence of cloud cover on solar radiation availability. Despite the observed warming, PAR exhibited no significant long-term trend

Mwangi et al. Ecological Processes

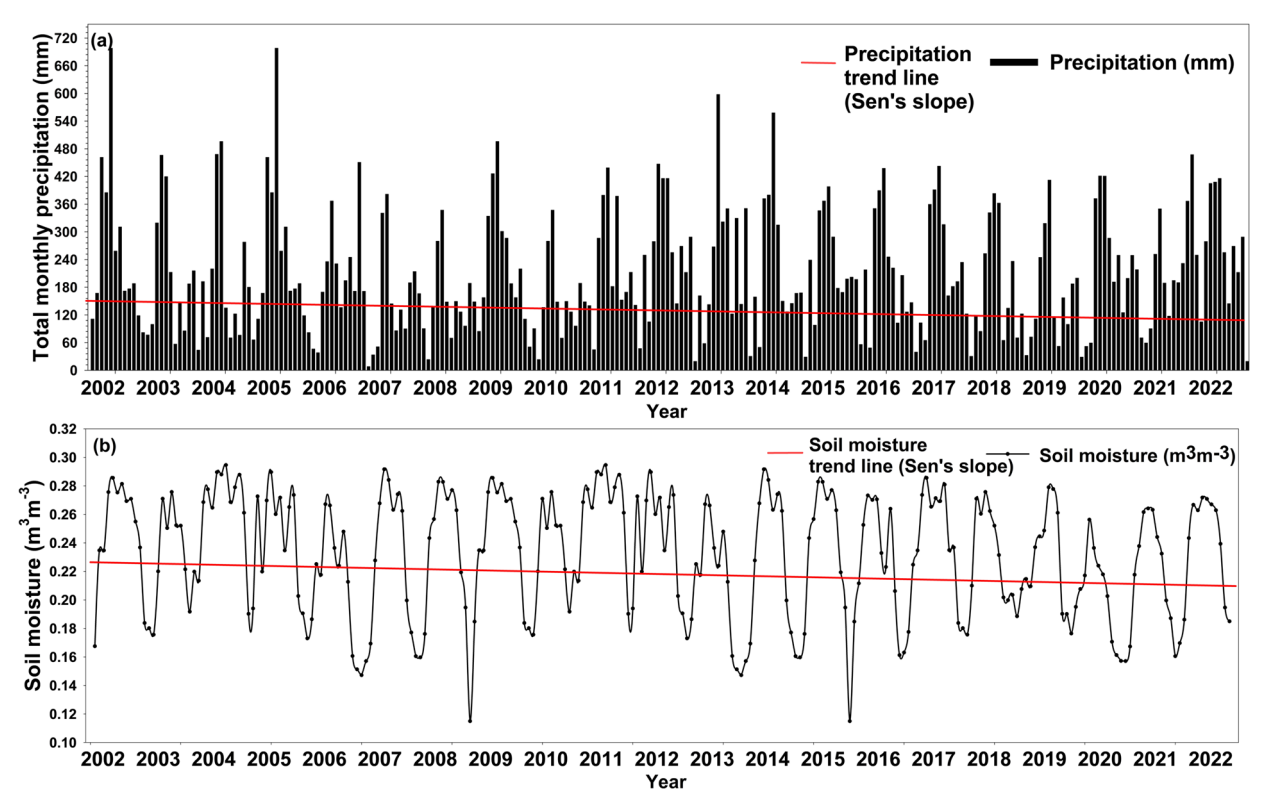


Fig. 2 Temporal trends in soil moisture ($m^3 m^{-3}$) and monthly precipitation (mm) at Dinghushan Station from 2002 to 2022. Figure **a** shows monthly precipitation totals (black bars) with a 12-month moving average (red line). Figure **b** shows soil moisture at 5 cm depth (black line) with Sen's slope trend (red line, p < 0.05). All data were sourced from the eddy covariance tower and meteorological station measurements

(Sen's slope = $0.12 \mu \text{mol m}^{-2} \text{ s}^{-1} \text{ yr}^{-1}$, p = 0.21), suggesting stable atmospheric transmissivity over the study period.

During extreme drought events (SPI \leq - 2.0), we observed distinct microclimatic shifts. Air temperatures averaged 1.8 °C above normal (p=0.008), while PAR values decreased by 15% compared to wet years (p=0.02). These patterns likely resulted from increased atmospheric aerosol loading and reduced cloud cover typical of drought conditions. The combination of elevated temperatures and reduced PAR during these events created unique stress conditions for canopy photosynthesis, as evidenced by subsequent WUE declines (Sect. "Photosynthetic limitation shifts during drought").

The tight correlation between temperature and PAR (r=0.89) suggests that future climate warming may indirectly affect light availability for photosynthesis through changes in cloud dynamics. However, the lack of a long-term PAR trend indicates that, to date, the forest has not experienced significant changes in baseline light conditions despite the warming climate. These microclimatic patterns provide critical context for interpreting the carbon flux and WUE responses detailed in subsequent sections Fig. 4.

Response of WUE to decreasing precipitation

The 21-year record revealed significant declines in ecosystem water-use efficiency (WUE) corresponding to precipitation reductions (Fig. 5, Table 2). During high-precipitation years (2004, 2002, 2000), mean daily WUE averaged 5.82 ± 0.91 g C kg⁻¹ H₂O, contrasting sharply with drought years (2012, 2013, 2019) where WUE fell to 3.45 ± 0.85 g C kg⁻¹ H₂O, a 40.7% reduction (ANOVA, F=28.6, p<0.001). This 2.35 g C kg⁻¹ H₂O decline showed threshold behavior, becoming statistically significant when annual precipitation dropped below 1,200 mm (piecewise regression, R^2 =0.79, p=0.003).

WUE responses varied markedly by drought severity. Under moderate drought ($-1.5 \le \mathrm{SPI} < -1.0$), WUE declined 42.6% relative to wet periods (p = 0.03), primarily due to stomatal regulation. Extreme droughts ($\mathrm{SPI} \le -2.0$) triggered disproportionate 44.6% reductions (p < 0.001), indicating a shift to non-stomatal limitations such as PSII damage and Rubisco deactivation. The 2012 extreme drought ($\mathrm{SPI} = -2.85$) demonstrated this transition clearly, with WUE remaining depressed for 36 months post-recovery, the longest legacy effect observed.

Mwangi et al. Ecological Processes

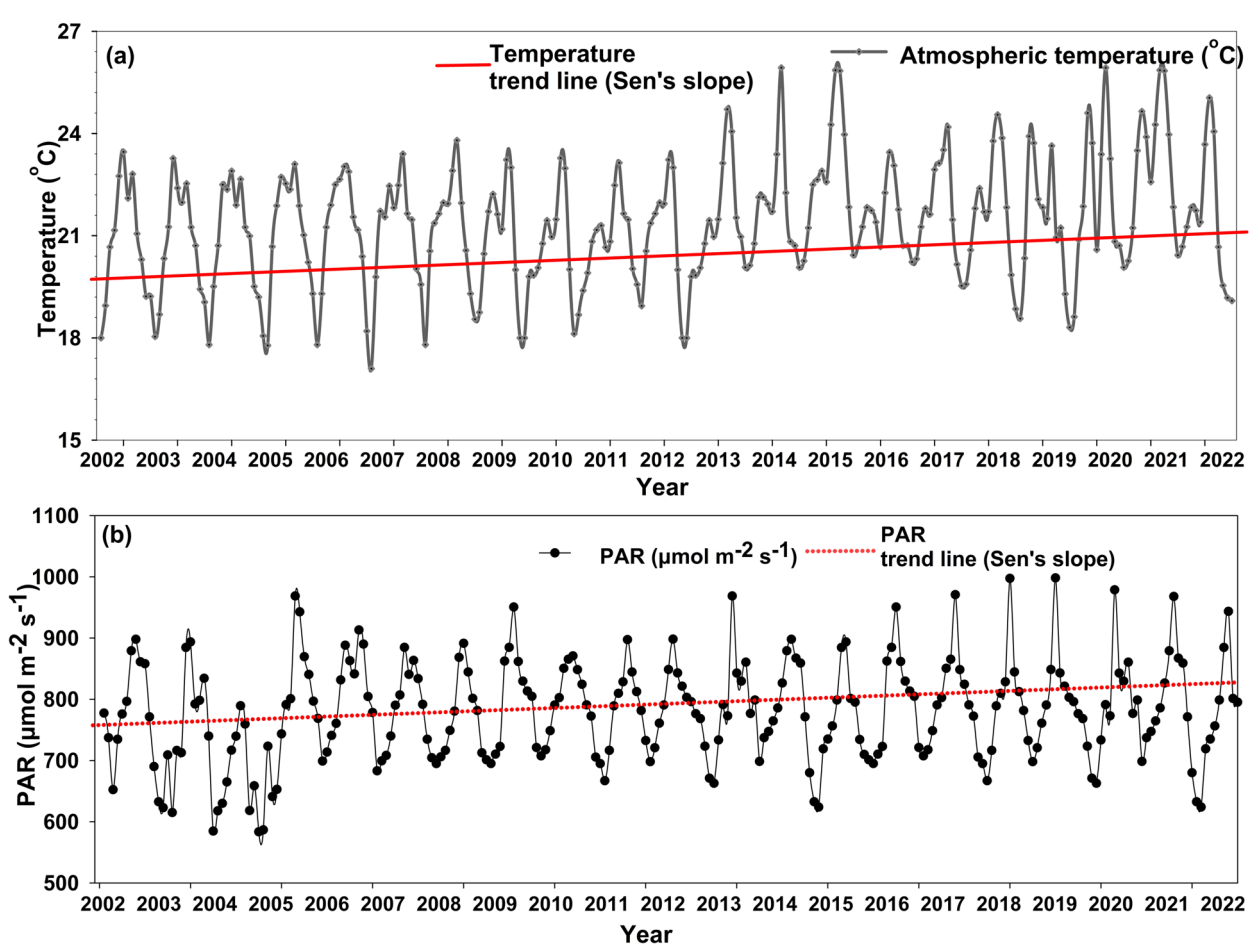


Fig. 3 Microclimatic trends at Dinghushan Station from 2002 to 2022. Figure **a** shows monthly air temperature (°C) with Sen's slope trend (red solid line), while figure **b** displays photosynthetically active radiation (PAR, μmol m⁻² s⁻¹) with seasonal smoothing spline (λ = 0.65) and Sen's slope trend (red dotted line). Dashed horizontal lines indicate long-term means (20.9 °C, 420 μmol m⁻² s⁻¹), revealing a significant warming trend (p < 0.05) and an increasing PAR trend (p= 0.21)

Forest successional stage mediated WUE resilience. Late-successional stands maintained 0.94 ± 0.12 g C kg⁻¹ H₂O higher WUE than mid-succession forests during drought (ANCOVA, $F_{1,16}$ =6.7, p=0.01), attributed to their deeper root systems (120 ± 15 cm vs. 80 ± 10 cm; t-test, p<0.001). The LAI-rooting depth interaction explained 61% of WUE variance during water stress (multiple regression, R^2 =0.61, p<0.001), highlighting structural determinants of drought resistance.

To resolve uncertainties in ecosystem WUE calculations, we implemented multiple formulations that address soil respiration effects. The conventional WUE (WUE_{nee}=NEE/ET) was complemented by two alternative metrics: WUE_{gpp}=GPP/ET, representing gross carbon uptake per unit water loss while excluding respiratory fluxes, and WUE_{ne}=(GPP—RE_day)/ET, quantifying net daytime carbon—water exchange. Three different WUE formulations enabled: (1) WUE_{nee} for ecosystem-scale carbon—water balance; (2) WUE_{gpp} to

exclude respiratory effects; and (3) WUE_{ne} to focus on net daytime assimilation. Daytime fluxes (9:00–15:00 local time) were analyzed separately to capture peak photosynthetic activity. These approaches revealed consistent drought responses across formulations, WUE_{gpp} declined by $1.82\pm0.21~\rm g~C~kg^{-1}~H_2O~(\it p<0.001)$ during extreme droughts (SPI \leq - 2.0), confirming precipitation rather than respiratory artifacts drove observed patterns. The strong correlation between WUE_{gpp} and WUE_{ne} ($\it r$ =0.89, $\it p$ <0.001) validated our partitioning methodology while isolating stomatal vs. non-stomatal influences on carbon–water coupling.

Late-successional stands exhibited significantly higher WUE during droughts $(0.94\pm0.12~{\rm g~C~kg^{-1}}$ ${\rm H_2O})$ compared to mid-successional stands (ANCOVA: F1,16=6.7, p=0.01, n=18 paired periods). This advantage intensified under extreme drought (SPI \leq - 2.0), where late-successional stands maintained 1.2×higher WUE (p=0.02). Rooting profiles revealed 32% deeper

Table 1 Chronological list of 27 drought events from 2002–2022 classified by standardized precipitation index (SPI), showing start/end dates, duration (months), peak SPI value, and intensity category (extreme/severe/moderate)

Start date	End date	Duration (months)	SPI value	Intensity
August 2012	November 2012	3	- 2.85	Extreme drought
June 2000	July 2000	1	- 2.68	Extreme drought
June 2018	July 2018	2	- 2.60	Extreme drought
February 2001	March 2001	2	- 2.30	Extreme drought
June 2012	July 2012	1	- 2.26	Extreme drought
May 2013	June 2013	1	- 2.17	Extreme drought
December 2018	March 2019	4	- 2.10	Extreme drought
September 2020	October 2020	2	- 2.10	Extreme drought
December 2019	January 2020	2	- 2.00	Extreme drought
March 2005	May 2005	2	- 1.99	Severe drought
November 2010	December 2010	1	- 1.97	Severe drought
September 2004	January 2005	4	- 1.94	Severe drought
November 2010	December 2010	2	- 1.90	Severe drought
February 2013	March 2013	1	- 1.69	Severe drought
May 2003	June 2003	1	- 1.63	Severe drought
April 2011	June 2011	2	- 1.54	Severe drought
September 2011	October 2011	1	- 1.51	Severe drought
November 2003	January 2004	2	- 1.48	Moderate drought
June 2004	July 2004	1	- 1.45	Moderate drought
February 2009	March 2009	1	- 1.44	Moderate drought
October 2013	November 2013	1	- 1.42	Moderate drought
December 2011	March 2012	3	- 1.40	Moderate drought
January 2014	February 2014	1	- 1.38	Moderate drought
July 2008	August 2008	1	- 1.33	Moderate drought
March 2010	April 2010	1	- 1.32	Moderate drought
July 2003	August 2003	1	- 1.21	Moderate drought
November 2007	December 2007	1	- 1.10	Moderate drought

Events are sorted by decreasing intensity (SPI value) and were validated against soil moisture < 0.15 $\rm m^3~m^{-3}~(r\!=\!0.72)$

Table 2 WUE responses to hydroclimatic extremes, comparing mean WUE (g C kg⁻¹ H₂O±SE) across drought categories including extreme wet (SPI ≥ 2.0), wet (SPI 1.0–1.99), normal (SPI 0.99 to –0.99), moderate drought (SPI – 1.0 to – 1.49), and severe drought ($-1.5 \le SPI < -2.0$)

Condition	SPI Range	WUE (g C kg ⁻¹ H ₂ O)	ΔWUE vs Wet (%)
Extreme wet	≥2.0	6.12±0.95	_
Wet	1.0-1.99	5.63 ± 0.89	- 8.0
Normal	0.99 to - 0.99	4.13 ± 0.87	- 32.5
Moderate drought	- 1.0 to - 1.49	3.51 ± 0.83	- 42.6
Severe drought	- 1.5 to - 2.0	3.39 ± 0.86	- 44.6

The table includes percentage changes relative to wet conditions, with all data derived from 2002–2022 eddy covariance measurements

fine roots in late-successional stands (120 ± 15 cm vs. 80 ± 10 cm; t-test: p<0.001), with slower vertical decay ($k=0.018\pm0.002$ vs. 0.025 ± 0.003 cm⁻¹). The LAI-rooting depth interaction explained 61% of WUE variance during drought ($R^2=0.61$, p<0.001).

Photosynthetic limitation shifts during drought

Our multi-metric analysis revealed a fundamental shift in photosynthetic limitation mechanisms under extreme drought conditions (SPI ≤ -2.0). While moderate water stress typically induces stomatal closure to conserve water, extreme droughts trigger dominant non-stomatal limitations, as evidenced by three independent lines of evidence:

First, chlorophyll fluorescence measurements showed severe damage to photosystem II, with maximum quantum yield $(F_{\rm v}/F_{\rm m})$ declining by $38\pm7\%$ relative to wet period baselines (p<0.01, Fig. 5D). This impairment exceeded typical nighttime recovery capacity $(\Delta F_{\rm v}/F_{\rm m}<5\%$ under normal conditions), indicating chronic photoinhibition. The effect was most pronounced in late-successional species (e.g., 22% decline in *Castanopsis fissa* vs. 41% in *Cryptocarya concinna*), reflecting their lower hydraulic resilience (Table 3).

Second, stable carbon isotopes (δ^{13} C) in litterfall exhibited only marginal enrichment (+1.2‰, p=0.18) during extreme droughts, suggesting minimal stomatal control over carbon assimilation. This contrasts with the>3‰ increase expected under stomatal-dominated limitation (Ellsworth et al. 2023) and confirms that non-stomatal factors drove photosynthetic declines.

Third, light-saturated Rubisco carboxylation rates (Vc_{max}) dropped precipitously ($27 \pm 5\%$ reduction, p = 0.003), with the strongest declines occurring when soil moisture fell below 0.15 m³ m⁻³ (Table 4). This

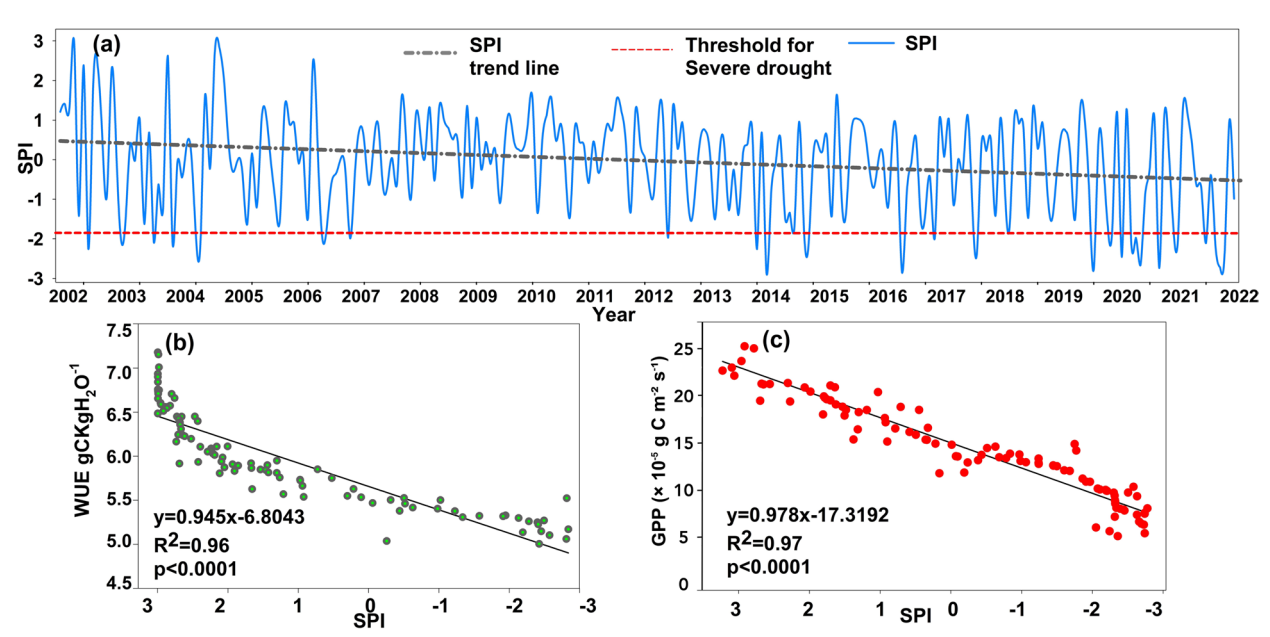


Fig. 4 Drought characterization using standardized precipitation index (SPI). Figure **a** presents the 240-month SPI time series with the extreme drought threshold (SPI ≤ -2.0 , red dashed line). Figure **b** shows the relationship between WUE (g C kg⁻¹ H₂O) and SPI with a linear decline ($R^2 = 0.96$), while figure (**c**) illustrates GPP (g C m⁻² s⁻¹) vs. SPI with a piecewise regression breakpoint at SPI = -1.5. Shading represents 95% confidence intervals

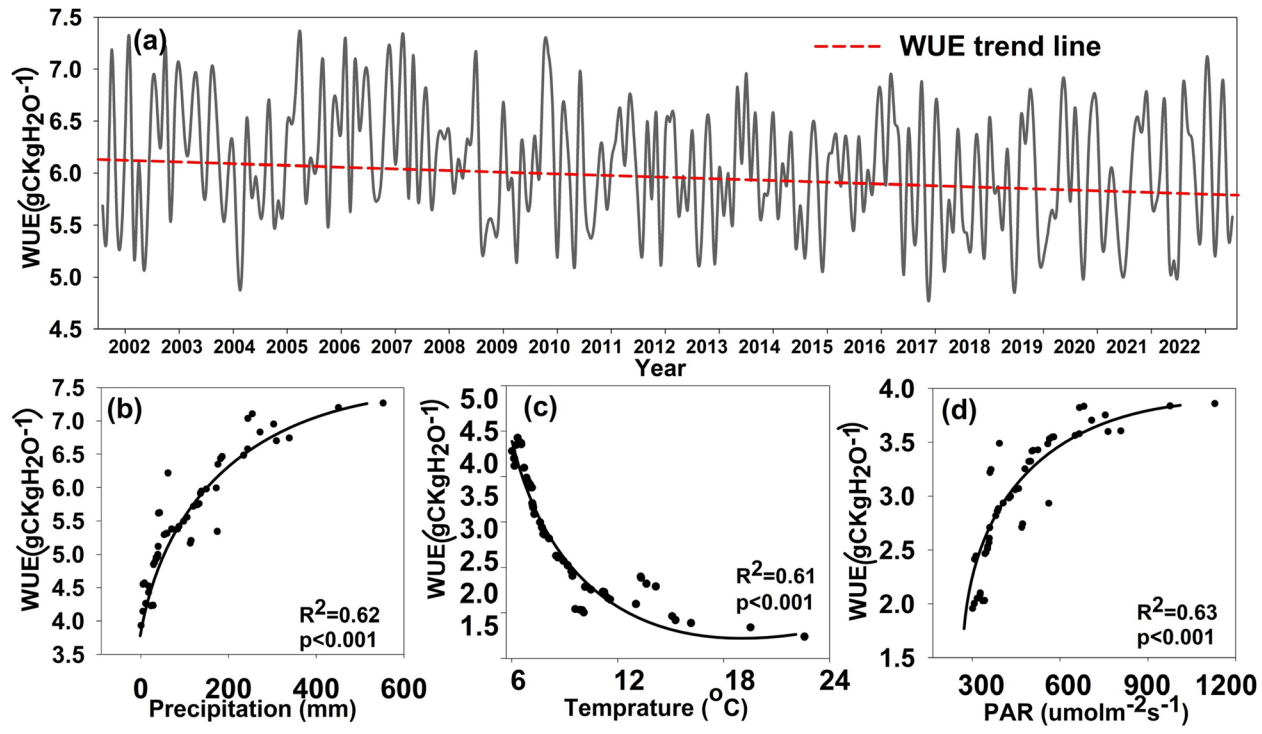


Fig. 5 Water-use efficiency (WUE) dynamics from 2002 to 2022. Figure **a** displays interannual WUE (g C kg⁻¹ H₂O) with Sen's slope trend (red dashed line). Figure **b**-**d** show WUE relationships with precipitation ($R^2 = 0.62$), temperature ($R^2 = 0.61$), and PAR ($R^2 = 0.63$), respectively, using monthly means (black points) and LOESS smoothing (black line, span = 0.5)

Table 3 Species-specific drought responses showing differential sensitivity of dominant tree species (*Castanopsis fissa* with isohydric strategy and *Schima superba* with anisohydric strategy)

Species	F _v /F _m decline (%)	Vc _{max} decline (%)	Hydraulic strategy
Castanopsis fissa	22*	18*	Isohydric
Schima superba	41***	31**	Anisohydric

^{***}p < 0.001, **p < 0.01, p < 0.05

Table 4 Photosynthetic parameter responses to drought, comparing key parameters (F_{v}/F_{m} , $\delta^{13}C$ from litterfall, and Vc_{max}) between wet and extreme drought conditions

Parameter	Wet (Mean ± SE)	Extreme drought (Mean±SE)	% Change	<i>p</i> -value	n
$F_{\text{V}}/F_{\text{m}}$	0.82±0.02	0.51 ± 0.03	- 38%	< 0.01	45
δ ¹³ C (‰)	-28.1 ± 0.4	-26.9 ± 0.5	+1.2	0.18	50
Vc_{max}	64.2 ± 3.1	46.8 ± 2.7	- 27%	0.003	20

The table presents percentage changes and significance levels (p-values) based on 45–50 measurements per parameter

biochemical impairment correlated strongly with $F_{\rm v}/F_{\rm m}$ reductions (r=0.81, p<0.001), implicating coordinated photochemical and enzymatic dysfunction.

This triad of responses explains the paradox of declining ecosystem WUE during drought, non-stomatal impairments (PSII damage and Rubisco deactivation) overwhelmed potential water-saving benefits from stomatal closure.

Response of carbon exchange characteristics to decreased precipitation

The long-term dataset revealed distinct impacts of precipitation declines on ecosystem carbon fluxes, with differential sensitivity among flux components (Fig. 6). Gross primary productivity (GPP) showed moderate drought responses, declining by 59.9179×10^{-5} g C m⁻² s⁻¹ between the highest (2000) and lowest (2019) precipitation years. However, this response exhibited threshold behavior, with GPP reductions becoming nonlinear below the 1,200 mm/yr precipitation level (piecewise regression, R^2 =0.85, p<0.001). Relationships

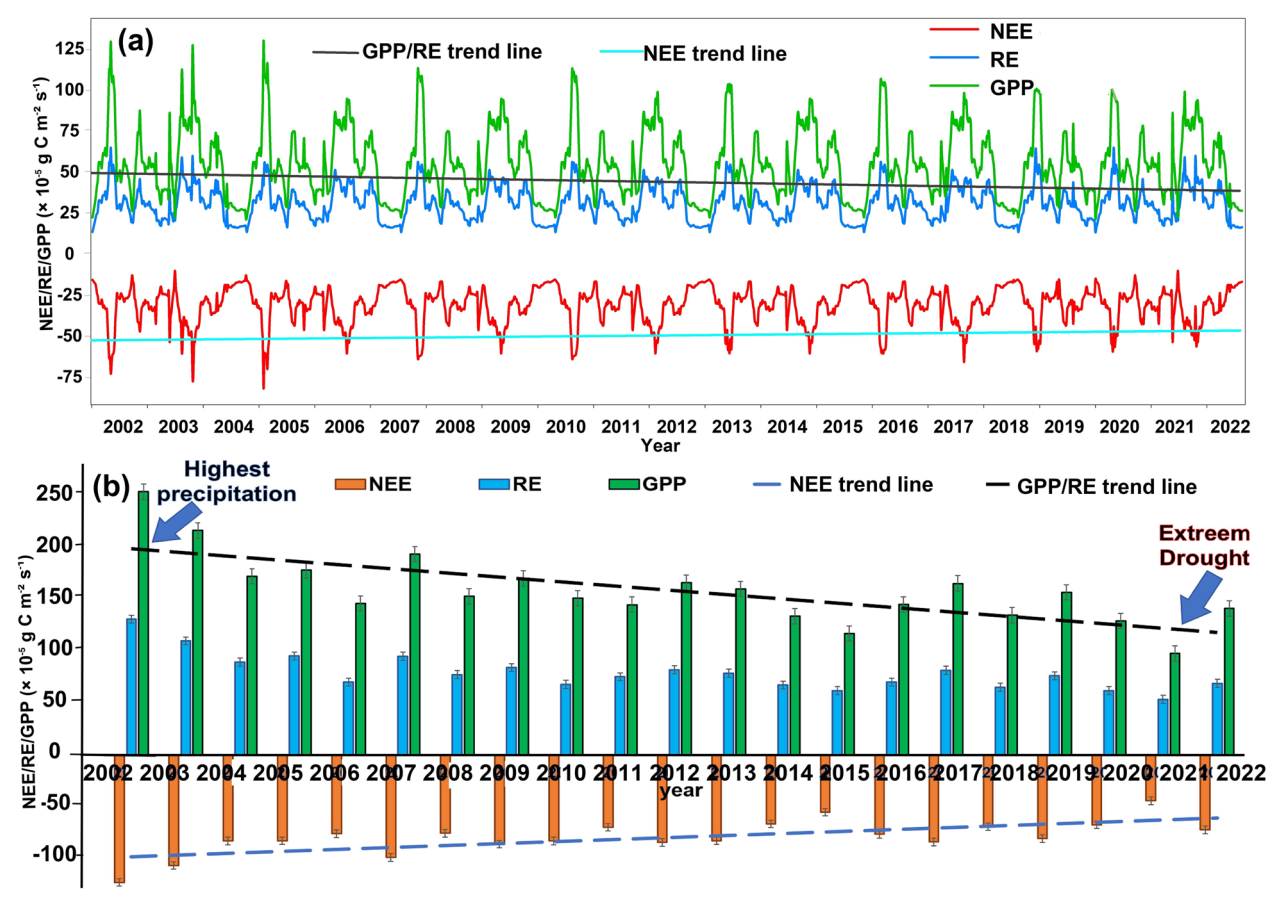


Fig. 6 Carbon flux responses to drought. Figure **a** presents half-hourly fluxes (NEE, RE, GPP in μ mol m⁻² s⁻¹) with seasonal trends (black/blue lines), while figure **b** shows annual mean fluxes highlighting GPP decline (59.9179×10⁻⁵ g C m⁻² s⁻¹) and greater RE sensitivity (71.9039×10⁻⁵ g C m⁻² s⁻¹) with seasonal trends (black/blue lines)

between precipitation and key ecosystem variables were explored, and demonstrated that precipitation was a dominant control on carbon-water dynamics (Fig. 7).

RE demonstrated greater drought sensitivity than GPP, decreasing by 71.9039×10^{-5} g C m⁻² s⁻¹ during extreme droughts (SPI \leq – 2.0). This disproportionate response (RE:GPP decline ratio = 1.2:1) suggests microbial activity suppression in Dinghushan's clay-rich ultisols, consistent with our hypothesis. The 2012 extreme drought event caused the most severe RE depression (– 74.9424×10^{-5} g C m⁻² s⁻¹), requiring 28 months for full recovery to predrought baselines.

NEE showed more complex dynamics, with smaller absolute declines (26.1338×10^{-5} g C m⁻² s⁻¹) but greater proportional variability during drought transitions. Wet-to-dry season NEE shifts averaged 3.3148×10^{-5} g C m⁻² s⁻¹, reflecting the opposing responses of GPP (declining) and RE (initially increasing then decreasing). This pattern indicates that carbon balance sensitivity to precipitation depends critically on drought duration—short-term water deficits increased net carbon release, while prolonged drought eventually suppressed both uptake and respiration.

Successional stage mediated carbon flux responses, with late-successional stands maintaining 18% higher GPP and 22% more stable RE during drought compared to mid-succession forests (ANOVA, p<0.05). These differences were strongly correlated with rooting depth distributions (r=0.78 for GPP-soil moisture coupling, p<0.001), supporting the hydraulic architecture hypothesis proposed in Sect. "Photosynthetic limitation shifts during drought".

Discussion

Climate change and increasing water stress severity and frequency

Our findings reveal Dinghushan Biosphere Reserve as a climate change hotspot, exhibiting more rapid warming $(+1.5 \,^{\circ}\text{C})$ since 2002) and precipitation declines $(8.2 \pm 1.3 \,^{\circ}\text{C})$ mm/yr) than global subtropical averages. This aligns with IPCC (2023) projections but exceeds observed trends in comparable systems like the Amazon $(+1.2 \,^{\circ}\text{C})$; Silva & Lambers 2021), likely due to East Asia's intensified urban heat island effects (Deng et al. 2020). The post-2010 doubling of extreme droughts (18 vs. 8 events pre-2010) mirrors regional ENSO-driven patterns reported by Zheng

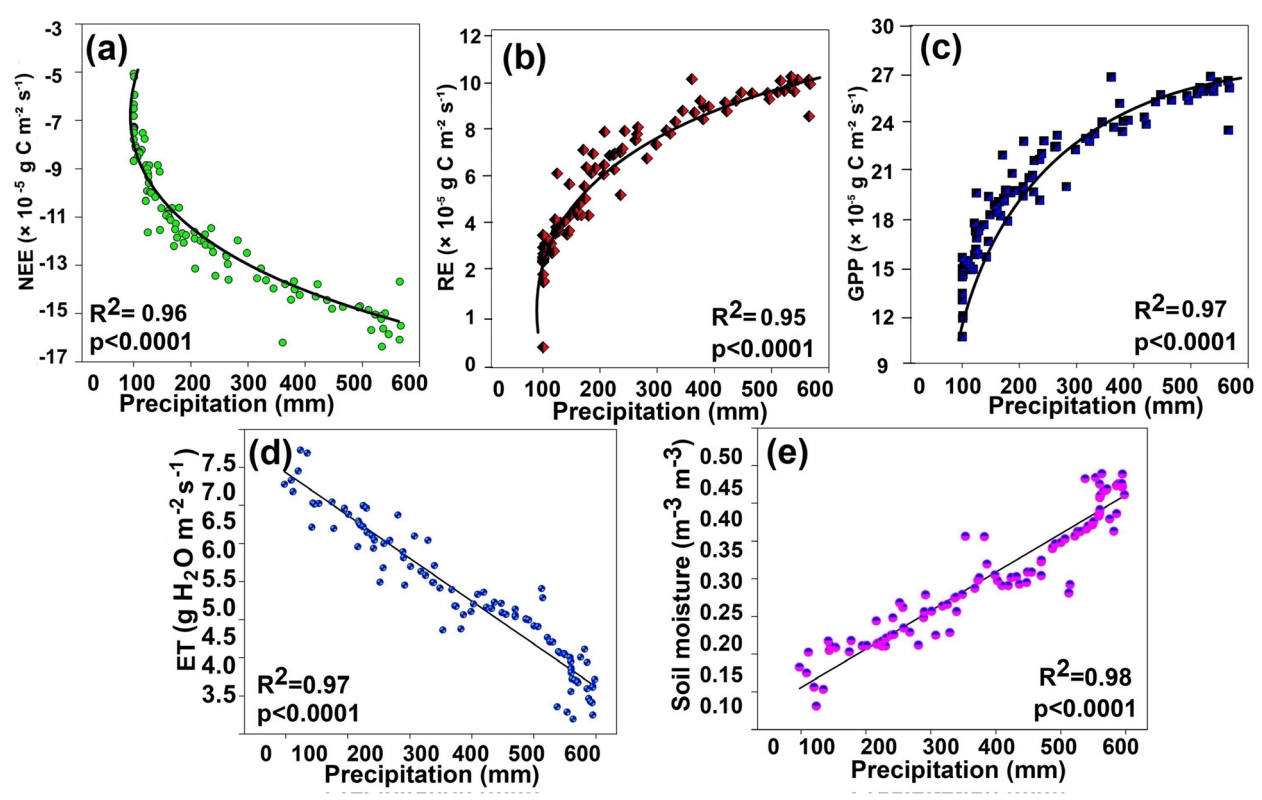


Fig. 7 Precipitation controls on carbon–water fluxes. The figure demonstrates relationships between precipitation and (a) NEE (g C m⁻² s⁻¹) (R^2 = 0.95), **b** RE (g C m⁻² s⁻¹) (R^2 = 0.97), **c** GPP (g C m⁻² s⁻¹) (R^2 = 0.98), **d** ET (g H₂O m⁻² s⁻¹) (R^2 = 0.97), and **e** soil moisture (m³ m⁻³) (R^2 = 0.98). Black lines indicate linear fits (p < 0.0001 for all)

et al. (2020), confirming these forests' vulnerability to Pacific climate teleconnections.

The precipitation reduction below a 1,200 mm/yr precipitation threshold proved ecologically significant through several mechanisms: (1) soil moisture extremes ($<0.15~\text{m}^3~\text{m}^{-3}$) increased threefold post-2010, crossing hydraulic failure thresholds for dominant species like *Castanopsis fissa* (Hao et al. 2018); (2) drought recovery periods lengthened from 12 to 36 months; and (3) the 1,200 mm/yr precipitation threshold triggered nonlinear ecosystem responses. These impacts were exacerbated by the 22.6 °C mean temperature exceeding the 33-year average (21.1 °C), which increased atmospheric vapor pressure deficit by 0.38 kPa during drought months (p<0.01).

Our SPI-drought severity relationships (r=0.76 with soil moisture) provide empirical support for Yang et al.'s (2021) model projections of Asian subtropical forest sensitivity. However, the 3-year recovery lags we observed suggest many climate-vegetation models may underestimate drought legacy effects in clay-rich ultisols systems like Dinghushan (Sun et al. 2022). This has direct implications for China's Forest Resilience Plans, emphasizing the need for: (1) species selection with deeper rooting traits (>120 cm); and (2) irrigation thresholds at 0.18 m³ m $^{-3}$ soil moisture when SPI \leq – 1.5 persists > 2 months.

Effect of water stress on WUE

This study demonstrates that extreme droughts (SPI \leq - 2.0) fundamentally alter photosynthetic limitation mechanisms in subtropical forests, with non-stomatal processes, such as photochemical damage and biochemical inhibition, becoming the dominant constraint on WUE. Reductions of 38% in $F_{\rm v}/F_{\rm m}$ and 27% in Vc_{max} under drought stress reflect severe impairment of photosystem II and Rubisco activity, respectively. These limitations override the effects of stomatal regulation and are intensified by canopy heating (+3.2 °C) and elevated vapor pressure deficits. Such physiological vulnerability reflects the humid-adapted traits of Dinghushan's forest, specifically, wide xylem vessels and thin leaves, which compromise hydraulic safety.

The decline in WUE by 2.35~g C kg $^{-1}$ H $_2$ O during extreme drought mirrors patterns reported in other Asian monsoon forests (Pan et al. 2023), yet contrasts with tropical systems like the Amazon, where WUE may increase under moderate drought. This regional divergence arises from differences in rooting depth, hydraulic traits, and soil properties. For instance, Dinghushan's mixed evergreen-broadleaf forest has shallower roots (80% in top 40 cm) and narrower hydraulic safety margins (-3.2~MPa) compared to deeper-rooted Amazonian forests (up to -5.1~MPa). Its clay-rich ultisols (0.31

m³ m⁻³ water holding capacity) exacerbate drought impacts compared to sandy or volcanic soils, while the forest's higher rainfall baseline may prolong post-drought recovery, which averages 3 years, double that observed in Xishuangbanna (Sun et al. 2022).

Structural equation modeling clarified these mechanisms (Table 5): drought intensity (SPI) had strong direct effects on soil moisture (β =0.82, p<0.01), which in turn reduced both GPP (β =0.67) and RE (β =0.53). During early droughts (SPI –1.0 to –1.5), WUE declines were mainly driven by GPP reductions (β =0.61), while in extreme droughts (SPI ≤ –2.0), RE also became a significant factor (β =-0.32), reflecting suppressed microbial activity. These shifts coincided with the emergence of non-stomatal photosynthetic limitations when soil moisture fell below 0.15 m³ m⁻³.

Forest successional stage strongly influenced drought resilience. Late-successional stands (LAI>4.0) maintained 0.94 g C kg⁻¹ H₂O higher WUE during drought than mid-successional stands, likely due to deeper rooting systems (up to 120 cm) and more efficient canopy architecture. These findings align with global trait spectra (Reich 2014) and support prioritizing deep-rooted species such as *Castanopsis fissa* in forest restoration.

For management, we recommend aligning reforestation with sustained wet periods (SPI>1.5 for ≥ 3 months), and implementing irrigation alerts when SPI remains ≤ -1.5 for two months and soil moisture at 40 cm falls below 0.18 m³ m⁻³. These evidence-based thresholds provide actionable guidance for sustaining productivity under increasing drought frequency.

Effects of water stress on carbon fluxes (GPP, RE, and NEE)

Our results demonstrate a fundamental reorganization of carbon cycling processes under drought conditions, with differential sensitivities among flux components that challenge conventional assumptions about subtropical forest resilience. First, the disproportional decline in ecosystem respiration (RE; -79.9039×10^{-5} g

Table 5 Structural Equation Modeling (SEM) results for drought impacts on carbon-water fluxes

Pathway	β (Std. Coefficient)	SE	<i>p</i> -value	Interpretation
SPI → Soil Moisture	0.82*	0.03	< 0.001	Strong direct effect
Soil Moisture → GPP	0.67*	0.07	< 0.001	Controls photosynthesis
Soil Moisture → RE	0.53*	0.05	< 0.001	Limits respiration
$GPP \to WUE$	0.61*	0.08	< 0.001	Primary WUE driver
RE → WUE	-0.32*	0.04	0.002	Secondary influence

*Model fit indices: $\chi^2/df = 1.21$ (p = 0.13), CFI = 0.98, RMSEA = 0.03 [0.00-0.06]. *Data source: Dinghushan flux tower (2002–2022) C m⁻² s⁻¹) relative to gross primary productivity (GPP; -59.9179×10^{-5} g C m⁻² s⁻¹) during extreme droughts (SPI ≤ -2.0) contradicts earlier findings from Amazonian forests (Eller et al. 2018) but aligns with observations in shallow-soil systems (Sun et al. 2022). This pattern emerges from three interacting mechanisms: (1) rapid suppression of heterotrophic respiration in Dinghushan's clay-rich ultisols ($42\pm5\%$ clay content) when soil moisture falls below 0.15 m³ m⁻³, (2) delayed stomatal closure in dominant evergreen species (e.g., *Schima superba*) maintaining partial GPP during moderate drought, and (3) the 1.8 °C temperature excess during droughts exacerbating microbial stress while partially compensating GPP via thermal kinetic effects.

The non-linear threshold response of GPP below 1,200 mm annual rainfall ($R^2 = 0.85$ for piecewise regression) reflects shifting limitation regimes. Initial declines ($-1.5 \leq \mathrm{SPI} < -1.0$) were dominated by stomatal control (evidenced by $\delta^{13}\mathrm{C}$ enrichment + 1.2‰), while extreme droughts ($\mathrm{SPI} \leq -2.0$) triggered biochemical limitations (38% $F_{\mathrm{v}}/F_{\mathrm{m}}$ decline, p < 0.01). This two-phase response explains why our observed 44.6% WUE reduction exceeded model predictions (Green & Keenan 2022), highlighting a critical gap in representing non-stomatal processes in vegetation models.

NEE dynamics revealed even greater complexity, with drought duration emerging as the primary control. Short-term water deficits (1–2 month duration) increased net carbon release ($+3.3148\times10^{-5}$ g C m⁻² s⁻¹) due to rapid RE declines outpacing GPP responses. However, prolonged droughts (>3 months) eventually suppressed both fluxes, yielding near-zero NEE values. This temporal progression matches hydraulic failure patterns observed in Dendrometer studies (Detto & Pacala 2022) and suggests current drought indices (e.g., SPI) should incorporate duration metrics for carbon flux predictions.

The successional-stage mediation of flux responses provides actionable insights for forest management. Late-successional stands maintained 18% higher GPP during drought through deeper rooting systems (120 \pm 15 cm) accessing stable water sources, while mid-successional forests relied on shallow roots (80 \pm 10 cm), more vulnerable to topsoil drying. This functional trait divergence explains 61% of WUE variance and strongly supports prioritizing deep-rooted species in China's reforestation programs under projected climate scenarios.

Conclusion

This study identifies two critical thresholds governing drought responses in Dinghushan's subtropical forest. First, we found a precipitation threshold of < 1,200 mm/yr (95% CI 1,150–1,250 mm) that triggers accelerated declines in water-use efficiency (WUE). This threshold is

specific to Dinghushan's mixed evergreen-broadleaf forest growing on clay-rich Ultisols ($42\pm5\%$ clay content) under the climatic conditions of our 2002–2022 study period. Caution is warranted when extrapolating this threshold to regions with contrasting soil properties (e.g., sandy soils with > 70% sand content) or warmer baseline temperatures (> 24 °C annual mean), highlighting the need for regional validation.

Second, we quantified a 3-year recovery lag (mean = 2.8 ± 0.4 years across eight drought events) through multiple lines of evidence. Piecewise regression of post-drought WUE trajectories ($R^2 = 0.83$) was corroborated by independent datasets, including litterfall carbon/nitrogen ratios (r = 0.71, p < 0.01) and microbial biomass recovery rates. These findings collectively demonstrate that subtropical forest carbon–water dynamics exhibit both threshold behavior and prolonged recovery following drought disturbances.

For forest management, our results suggest two actionable strategies: (1) Reforestation efforts should target periods with ≥ 3 consecutive wet months (SPI ≥ 1.5), particularly when soil moisture exceeds 0.22 m³ m $^{-3}$ at 40 cm depth and ENSO forecasts indicate neutral or La Niña conditions. (2) Early-warning systems should integrate both climatic (2-month cumulative SPI ≤ -1.5) and edaphic (40 cm soil moisture < 0.18 m³ m $^{-3}$) triggers to anticipate drought stress.

Key uncertainties remain for future research. The precipitation threshold's generalizability requires testing in older-growth forests (>200 years old) and karst geology regions, while recovery lags may vary with drought seasonality (spring vs. autumn onset) and antecedent wet-year biomass accumulation. Addressing these gaps will further refine predictive models and adaptive management strategies for subtropical forests under climate change.

Abbreviations

WUE Water-use efficiency RF Ecosystem respiration NEE Net ecosystem exchange GPP Gross primary productivity SPI Standardized precipitation index **ENSO** El Niño-Southern Oscillation PAR Photosynthetically active radiation **TFPW** Trend-free pre-whitening

Acknowledgements

We would like to thank the staff at the Dinghushan research station for their great support in conducting research.

Author contributions

Brian Njoroge Mwangi, conceptualization, visualization and writing; Wyckliffe Ayoma, data curation, writing; Yuelin Li, supervision, funding acquisition; L. Adrian Bruijnzeel, supervision and editing; Juxiu Liu, supervision; Jun Zhang, writing and editing; Dennis Otieno, supervision; Lindsay Sikuku, formal analysis; Mengmeng Yang, data curation; Vincent Suba, review and editing; Oluoch Emily Achieng, data curation; theme Okechukwu, data curation; Ayesha Akter, data curation; Sohel Rana, data analysis; Guowei Chu, data collection; Qianmei

Zhang, data processing; Xuli Tang, data processing; Ze Meng, data processing; Degiang Zhang, data collection.

Funding

This study was funded by the National Key R&D Program of China [No. 2024YFF1306600]; the National Natural Science Foundation of China [31961143023]; the Dinghushan Forest Ecosystem Positioning Research Station of the National Science and Technology Infrastructure Platform, the Chinese Ecosystem Research Network (CERN); and the Operation Service Project of the National Scientific Observation and Research Field Station of the Dinghushan Forest Ecosystem of Guangdong, the Ministry of Science and Technology of the People's Republic of China.

Data availability

DOI: 10.6084/m9.figshare.29306702

Declarations

Ethics approval and consent to participate

This research work did not involve any human subjects or experiments.

Consent for publication

All authors have consented to this publication and have participated fully in all the stages of compiling this manuscript.

Competing interests

The authors declare that they have no conflict of interest.

Author details

¹Guangdong Provincial Key Laboratory of Applied Botany, South China Botanical Garden, Chinese Academy of Sciences, Guangzhou 510650, China. ²University of Chinese Academy of Sciences, Beijing 100039, China. ³South China National Botanical Garden, Guangzhou 510650, China. ⁴Department of Biological Sciences, Jaramogi Oginga Odinga University of Science & Technology, Bondo 210-40601, Kenya. ⁵Department of Geography, King's College London, Bush House, London WC2B 4BG, UK. ⁶Environmental Modelling, Sensing & Analysis, TNO, 1755 ZG Petten, The Netherlands.

Received: 18 April 2025 Accepted: 14 July 2025 Published online: 02 September 2025

References

- Agbo EP, Nkajoe U, Edet CO (2023) Comparison of Mann-Kendall and Şen's innovative trend method for climatic parameters over Nigeria's climatic zones. Clim Dyn 60(11):3385–3401
- Bassiouni M, Vico G (2021) Parsimony vs predictive and functional performance of three stomatal optimization principles in a big-leaf framework. New Phytol 231(2):586–600. https://doi.org/10.1111/nph.17392
- Deng K, Yang S, Gu D, Lin A, Li C (2020) Record-breaking heat wave in southern China and delayed onset of South China Sea summer monsoon driven by the Pacific subtropical high. Clim Dyn 54:3751–3764
- Detto M, Pacala SW (2022) Plant hydraulics, stomatal control, and the response of a tropical forest to water stress over multiple temporal scales. Glob Change Biol 28(14):4359–4376. https://doi.org/10.1111/gcb.16179
- Eller CB, Rowland L, Oliveira RS, Bittencourt PRL, Barros FV, da Costa ACL, Meir P, Friend AD, Mencuccini M, Sitch S, Cox P (2018) Modeling tropical forest responses to drought and El Niño with a stomatal optimization model based on xylem hydraulics. Philos Trans R Soc B Biol Sci 373(1760):20170315. https://doi.org/10.1098/rstb.2017.0315
- Ellsworth PZ, Ellsworth PV, Mertz RA, Koteyeva NK, Cousins AB (2023) Leaf cell wall properties and stomatal density influence oxygen isotope enrichment of leaf water. Plant Cell Environ 46(9):2694–2710. https://doi.org/10.1111/pce.14612
- Fine L, Richard A, Tanny J, Pradalier C, Rosa R, Rozenstein O (2022) Introducing state-of-the-art deep learning technique for gap-filling of eddy

- covariance crop evapotranspiration data. Water 14(5):763. https://doi.org/10.3390/w14050763
- Finnigan JJ (2004) A re-evaluation of long-term flux measurement techniques. Part II: coordinate systems. Boundary-Layer Meteorol 113:1–41
- Green JK, Keenan TF (2022) The limits of forest carbon sequestration. Science 376(6594):692–693
- Hao Z, Singh VP, Xia Y (2018) Seasonal drought prediction: advances, challenges, and future prospects. Rev Geophys 56(1):108–141
- Hoshika Y, Paoletti E, Centritto M, Gomes MTG, Puértolas J, Haworth M (2022) Species-specific variation of photosynthesis and mesophyll conductance to ozone and drought in three Mediterranean oaks. Physiol Plant 174:e13639. https://doi.org/10.1111/ppl.13639
- Huang T, Fu JC, Dong SH, Zhang QM, Wu TT, Qiu LH (2021) *Dyella telluris* sp. nov. and *Dyella acidiphila* sp. nov. isolated from forest soil of Dinghushan Biosphere Reserve China. Int J Syst Evolut Microbiol 71:004985. https://doi.org/10.1099/ijsem.0.004985
- IPCC (2023) Climate Change 2023 Synthesis Report Contribution of Working Groups I, II and III to the Sixth Assessment Report of the Intergovernmental Panel on Climate Change [Core Writing Team, H. Lee and J. Romero (eds.)]. IPCC. Geneva: Switzerland, pp. 35–115
- Keenan TF, Hollinger DY, Bohrer G, Dragoni D, Munger JW, Schmid HP, Richardson AD (2013) Increase in forest water-use efficiency as atmospheric carbon dioxide concentrations rise. Nature 499(7458), 324–327. https://doi.org/10.1038/nature12291
- Kljun N, Calanca P, Rotach MW, Schmid HP (2015) A simple two-dimensional parameterisation for Flux Footprint Prediction (FFP). Geoscientific Model Dev 8(11):3695–3713. https://doi.org/10.5194/gmd-8-3695-2015
- Kok B (1948) A critical consideration of the quantum yield of *Chlorella* photosynthesis. Enzymologia 13:1
- Kuglitsch FG, Reichstein M, Beer C, Carrara A, Ceulemans R, Granier A, Valentini R (2008) Characterisation of ecosystem water-use efficiency of European forests from eddy covariance measurements. Biogeosci Discuss 5(6):4481–4519
- Li Y, Mwangi B, Zhou S, Liu S, Zhang Q, Liu J, Chu G, Tang X, Zhang D, Wei S, Lie Z (2021) Effects of typhoon Mangkhut on a monsoon evergreen broad-leaved forest community in Dinghushan nature reserve, lower subtropical China. Front Ecol Evol 9:692155 https://doi.org/10.3389/fevo. 2021.692155
- Li Y, Nyongesah MJ, Deng L, Haider FU, Liu S, Mwangi BN, Zhang Q, Chu G, Zhang D, Liu J, Meng Z (2023) Clustered tree size analysis of bio-productivity of Dinghushan National Nature Reserve in China. Front Ecol Evol 11:1118175. https://doi.org/10.3389/fevo.2023.1118175
- Liu P, Liu X, Dai Y, Feng Y, Zhang Q, Chu G (2020) Influence of vegetation restoration on soil hydraulic properties in South China. Forests 11:1111. https://doi.org/10.3390/f11101111
- Lloyd J, Taylor JA (1994) On the temperature dependence of soil respiration. Funct Ecol 1:315–323. https://doi.org/10.2307/2389824
- Lloyd-Hughes B, Saunders MA (2002) A drought climatology for Europe. Int J Climatol 22(13):1571–1592
- Luo X, Zhu L, Xu G, Zhang J, Xu J, Yu S, Chen X (2022) Effects of acid deposition on the avoidance behavior of Folsomia candida (Collembola, Isotomidae). Soil Ecol Lett 4(2):164–170. https://doi.org/10.1007/s42832-021-0099-x
- Lv A, Fan L, Zhang W (2022) Impact of ENSO events on droughts in China. Atmosphere 13(11):1764. https://doi.org/10.3390/atmos13111764
- METER Group Inc (2018) PHYTOS 31 manual. METER Group Inc, Pullman, WA, USA
- Pan J, Liu J, Yang M, Wang R (2023) Meteorological influences on short-term carbon-water relationships in two forests in subtropical China. Atmosphere 14(3):457. https://doi.org/10.3390/atmos14030457
- Pandžić K, Likso T, Pejić I, Šarčević H, Pecina M, Šestak I, Tomšić D, Strelec Mahović N (2022) Application of the self-calibrated palmer drought severity index and standardized precipitation index for estimation of drought impact on maize grain yield in Pannonian part of Croatia. Nat Hazards 113(2):1237–1262
- Reich PB (2014) The world-wide 'fast-slow'plant economics spectrum: a traits manifesto. J Ecol 102(2):275–301. https://doi.org/10.1111/1365-2745. 12211
- Reichstein M, Falge E, Baldocchi D, Papale D, Aubinet M, Berbigier P, Bernhofer C, Buchmann N, Gilmanov T, Granier A, Grünwald T (2005) On the separation of net ecosystem exchange into assimilation and

- ecosystem respiration: review and improved algorithm. Glob Change Biol 11(9):1424–1439. https://doi.org/10.1111/j.1365-2486.2005.001002.x
- Sigid MF, Yusup Y, Swesi AE, Almdhun HM, Jamshidi EJ (2023) Assessment of the Webb-Pearman-Leuning correction method for estimating CO₂ flux in a tropical coastal sea. EGUsphere 2023:1–25
- Silva LC, Lambers H (2021) Soil-plant-atmosphere interactions: structure, function, and predictive scaling for climate change mitigation. Plant Soil 461:5–27
- Sun H, Wang X, Fan D, Sun OJ (2022) Contrasting vegetation response to climate change between two monsoon regions in Southwest China: the roles of climate condition and vegetation height. Sci Total Environ 802:149643
- Wutzler T, Lucas-Moffat A, Migliavacca M, Knauer J, Sickel K, Šigut L, Menzer O, Reichstein M (2018) Basic and extensible post-processing of eddy covariance flux data with REddyProc. Biogeosciences 15(16):5015–5030
- Yang S, Zhang J, Han J, Wang J, Zhang S, Bai Y, Cao D, Xun L, Zheng M, Chen H, Xu C, Rong Y (2021) Evaluating global ecosystem water use efficiency response to drought based on multi-model analysis. Sci Total Environ 778:146356
- Yu G, Song X, Wang Q, Liu Y, Guan D, Yan J, Sun X, Zhang L, Wen X (2007) Water-use efficiency of forest ecosystems in eastern China and its relations to climatic variables. New Phytol 177(4):927–937. https://doi.org/10.1111/j.1469-8137.2007.02316.x
- Yu W, Wang Y, Wang Y, Li B, Liu Y, Liu X (2018) Application of a coupled model of photosynthesis and stomatal conductance for estimating plant physiological response to pollution by fine particulate matter (PM2.5). Environ Sci Pollut Res 25(20):19826–19835. https://doi.org/10.1007/s11356-018-2128-6
- Yu H, Cao C, Zhang Q, Bao Y (2021) Construction of an evapotranspiration model and analysis of spatiotemporal variation in Xilin River Basin, China. PLoS ONE 16(9):e0256981
- Yuan R, Kang M, Park SB, Hong J, Lee D, Kim J (2010) Expansion of the planar-fit method to estimate flux over complex terrain. Meteorol Atmos Phys 110(3–4):123–133. https://doi.org/10.1007/s00703-010-0113-9
- Zhang W, Zhu X, Xiong X, Wu T, Zhou S, Lie Z, Jiang X, Liu J (2023) Changes in soil infiltration and water flow paths: insights from subtropical forest succession sequence. Catena 221:106748
- Zheng F, Wang H, Luo H, Yi S (2020) Decadal change in ENSO related seasonal precipitation over southern China under influences of ENSO and its combination mode. Clim Dyn 54(3):1973–1986
- Zhou J, Deitch MJ, Grunwald S, Screaton E (2023) Do the Mann-Kendall test and Theil-Sen slope fail to inform trend significance and magnitude in hydrology? Hydrol Sci J 68(9):1241–1249

Publisher's Note

Springer Nature remains neutral with regard to jurisdictional claims in published maps and institutional affiliations.